Research Articles

Dual-Carbon Batteries

Large Interlayer Distance and Heteroatom-Doping of Graphite Provide New Insights into the Dual-Ion Storage Mechanism in Dual-Carbon Batteries

Xin Hu, Yitian Ma, Wenjie Qu, Ji Qian, Yuetong Li, Yi Chen, Anbin Zhou, Huirong Wang, Fengling Zhang, Zhengqiang Hu, Yongxin Huang,* Li Li, Feng Wu, and Renjie Chen*

Abstract: Dual-ion batteries (DIBs) is a promising technology for large-scale energy storage. However, it is still questionable how material structures affect the anion storage behavior. In this paper, we synthesis graphite with an ultra-large interlayer distance and heteroatomic doping to systematically investigate the combined effects on DIBs. The large interlayer distance of 0.51 nm provides more space for anion storage, while the doping of the heteroatoms reduces the energy barriers for anion intercalation and migration and enhances rapid ionic storage at interfaces simultaneously. Based on the synergistic effects, the DIBs composed of carbon cathode and lithium anode afford ultra-high capacity of 240 mAh g^{-1} at current density of 100 mA g^{-1}. Dual-carbon batteries (DCBs) using the graphite as both of cathode and anode steadily cycle 2400 times at current density of 1 A g^{-1}. Hence, this work provides a reference to the strategy of material designs of DIBs and DCBs.

[*] X. Hu, Prof. J. Qian, Y. Li, Y. Chen, A. Zhou, H. Wang, F. Zhang, Z. Hu, Y. Huang, L. Li, F. Wu, R. Chen
Beijing Key Laboratory of Environmental Science and Engineering, School of Material Science and Engineering, Beijing Institute of Technology
Beijing 100081 (China)
E-mail: huangyx@bit.edu.cn
    chenrj@bit.edu.cn

Prof. Y. Ma
School of Materials, Xi'an University of Science and Technology
Xi'an 710054 (China)

W. Qu
Shanghai Institute of Space Power-Sources
Shanghai 200245 (China)

Prof. J. Qian, Y. Huang, L. Li, F. Wu, R. Chen
Advanced Technology Research Institute, Beijing Institute of Technology
Jinan 250300 (China)

L. Li, F. Wu, R. Chen
Collaborative Innovation Center of Electric Vehicles in Beijing
Beijing 100081 (China)

Introduction

As the energy sources field progresses towards de-fossilization, clean energy, especially solar, wind, and tidal energies, has been rapidly exploited.[1] We need to develop large-scale energy storage devices with low cost and high sustainability synchronously to address the discontinuity and instability of renewable energy.[2] Lithium-ion batteries (LIBs) are one of the most widely used energy storage devices. However, the limited mineral resources and energy density limit the use of LIBs in large-scale energy storage.[3] Recently, advanced dual-ion batteries (DIBs) have been proposed. The working mechanism involves the respective intercalation of cations and anions into the anode and cathode during the charging/discharging process, which brings the benefits of high operating voltage and material availability to DIBs.[4] Furthermore, based on the dual-ion storage mechanism, dual-carbon batteries (DCBs), which use graphite as both cathode and anode, are considered as candidates for large-scale energy storage applications.[5]

Alongside the limited capacity, the sluggish ion diffusion kinetics and large volume deformation of the graphite electrode pose significant challenges for DIBs and DCBs.[6] At present, several ion intercalation models in graphite electrode have been proposed to describe different graphite intercalation compound (GIC) phases formed at various charge and discharge states, such as the Rudöff model and Daumus-Hérold model.[7] These models are presented based on the natural graphite structure with interlayer distance of 0.34 nm, indicating that the capacity brought by the ion insertion in the regular layer structure of graphite material has an upper limit.[8] Especially for anions, the PF$_6^-$ anion insertion in graphite to form C$_{16}$(PF$_6$) is calculated to have a capacity limit of 140 mAh g^{-1} with poor reversibility.[9]

In earlier works, various graphite materials were explored to reveal their ability of anion storage in different electrolytes. It was found that the electrochemical behaviors of anion storage in graphite are related to the exfoliation of materials and the formation of solid interface layers (SEI) on electrode surface. In this regard, Markle and co-workers found that the graphite with smaller size and lower crystallization exhibits better stability in polycarbonate (PC) based electrolyte at high voltage up to 5.5 V.[10] Recently, Tang and co-workers investigated the performances of graphite materials with different degrees of defect and particle sizes, such as locally ordered graphitized carbon and

natural graphite. The results indicated that the microscopic composition and structure have a significant effect on the anion storage capacity of graphite materials.[11] In addition, introduction of heteroatoms and design of nanoarchitectures of carbon material can effectively shorten its ion migration distance, enhance its electrical conductivity of electrode, and improve its reaction kinetics.[12] To date, the heteroatom-doping carbon materials with rich defects exhibited outstanding electrochemical performance to $Li^+/Na^+/K^+$ storage.[13] For instance, advanced graphitic carbon nitride ($g-C_3N_4$)-derived N-rich graphene exhibits excellent performance in sodium ion storage devices due to the large layer spacing created by heteroatom doping.[14]

In this work, a series of N-doping graphite with ultra-large interlayer distance (N-LIDGs) ranging from 0.39 to 0.51 nm were synthesized using a simple and scalable one-step catalytic method at different temperatures including 700, 800, and 900 °C. The ultra-large interlayer distance of N-LIDG-800 sample, that treated at temperature of 800 °C (labeled as N-LIDG-800), provides more spaces for anion storage, which enhances the specific capacity of DIBs dramatically. Additionally, the synergetic effect of heteroatom doping, which includes enhancing the adsorption energies of anions, reducing the migration barriers of anions, and optimizing the migration paths of anions, was confirmed through electrochemical analysis and theoretical calculations. As a consequence, a significant pseudocapacitive contribution combined with rapid anion intercalation of N-LIDGs were observed during the charging/discharging process in DIBs, generating a novel model of the anion storage process as a "deep-breathing" mechanism. Based on this novel model, the DIBs exhibited an ultra-high capacity of 240 mAh g^{-1} at a current density of 100 mA g^{-1} and cycled 200 times steadily. Furthermore, a novel pouch cell of DCBs with an appreciable capacity of 67 mAh g^{-1} at a current density of 250 mA g^{-1} was constructed. This work provides a facile and effective strategy to modify the surface and bulk structure of graphite as both of anode and cathode for DCBs, which can serve as a reference for other functional carbon materials for battery applications.

Results and Discussion

The N-LIDGs was prepared via one-step pyrolysis process of g-CN under the catalysis effect of metallic Zn powder as shown in Figure 1a.[15] In scanning electron microscope (SEM) image, the precursors of g-CN and metallic Zn microparticles were mixed homogeneously under manually grinding (Figure S1, Supporting Information). Under various temperature conditions, more pores can be observed in N-LIDG-800 and N-LIDG-900 samples compared to that of N-LIDG-700 (Figure S2 a–c, Supporting Information). Moreover, transition electron microscope images (TEM, as shown in Figure S3 a–c, Supporting Information) show that N-LIDG-700 exhibits a massive graphite particle-like morphology, while N-LIDG-800 and N-LIDG-900 are thin-layered graphene morphologies, that are consistent with the SEM images. In high-resolution TEM (HRTEM) images (as

shown in Figure 1 b–d, detailed in Figure S4, Supporting Information), the interlayer distances of different graphitic materials are 0.37, 0.51 and 0.39 nm of N-LIDG-700 (close to graphite of 0.335 nm), N-LIDG-800 and N-LIDG-900, respectively. Amongst, the large interlayer distance of 0.51 nm may provide more spaces for promoting migration of large-scale ions and enhancing adaptability of various anions. As shown in Figure 1e, the elemental mapping images of N-LIDG-800 demonstrate the homogeneous doping of N and O elements in carbon nanosheets with stoichiometric ratio of 18.01 % and 1.47 %, respectively (Figure S5 and Table S1, Supporting Information). The above results indicate the successful preparation of heteroatom doping of N-LIDGs. In addition, the Fourier transform infrared (FTIR) spectra and corresponding heatmap (Figure S6, Supporting Information) are employed to confirm the interaction between the carbon and nitrogen atoms in graphitic N-LIDG-800, which display a transmission peak at the range of 800–1750 cm^{-1} and illustrate the characteristic vibration bands of the C–N heterocycles.

To further verify the crystal structure, all as-prepared samples were detected using powder X-ray diffraction (XRD). The XRD patterns show that all three samples possess the characterized peak (002) which is close to the standard graphite (JCPDS No. 26-1079) located at 26.6° (Figure S7, Supporting Information). Interestingly, the (002) peaks of all samples are broadened because of the increase of disorder and the decrease of particle size. These broad peaks can confirm the amorphous state of three graphitic materials.[12a] However, the (002) peak of N-LIDG-800 moves towards the negative direction of 25.8°, indicating the enlarged interlayer distance which is consistent with the results in TEM images. Similarly, (002) peaks of N-LIDG-900 and N-LIDG-700 shift to 26.0° and 26.3°, which can be ascribed to enlarged interlayer distance.

Subsequently, the defect structure of N-LIDG-800 was detected via Raman spectroscopy as shown in Figure S8 (Supporting Information). A sharp G peak at 1580 cm^{-1} in the Raman spectra of N-LIDG-800 can be assigned to the in-plain vibration mode E2 g of sp^2 carbon atoms, indicating the typical graphite structure of N-LIDG-800. Meanwhile, a wide D peak at 1360 cm^{-1} induced by the A1 g vibration of C_6 rings demonstrates the existence of substantial defects in N-LIDG-800. The widely used indicator of I_D/I_G represents the defects in graphitic materials, and the large peak spacing further supports the existence of a short-range ordered structure.[16] The increased I_D/I_G value of 1.08 in N-LIDG-800 illustrates the presence of atom defects caused by abundant N atom doping, while maintaining the main structure of graphite.[17]

To confirm the chemical states of N-LIDG-700, N-LIDG-800 and N-LIDG-900, X-ray photoelectron spectroscopy (XPS) has been employed. As shown in the XPS survey spectrum (Figure S9a-c, Supporting Information), the obvious peaks are located at 285.3 eV, 399.6 eV and 532.4 eV corresponding to C 1s, N 1s and O 1s, respectively. Figure S9 exhibits the high-resolution spectrum of C 1s for three samples, and the peaks located at 284.5 eV, 286.1 eV and 288.0 eV are ascribed to C–C and C=C, C–N and C–O,
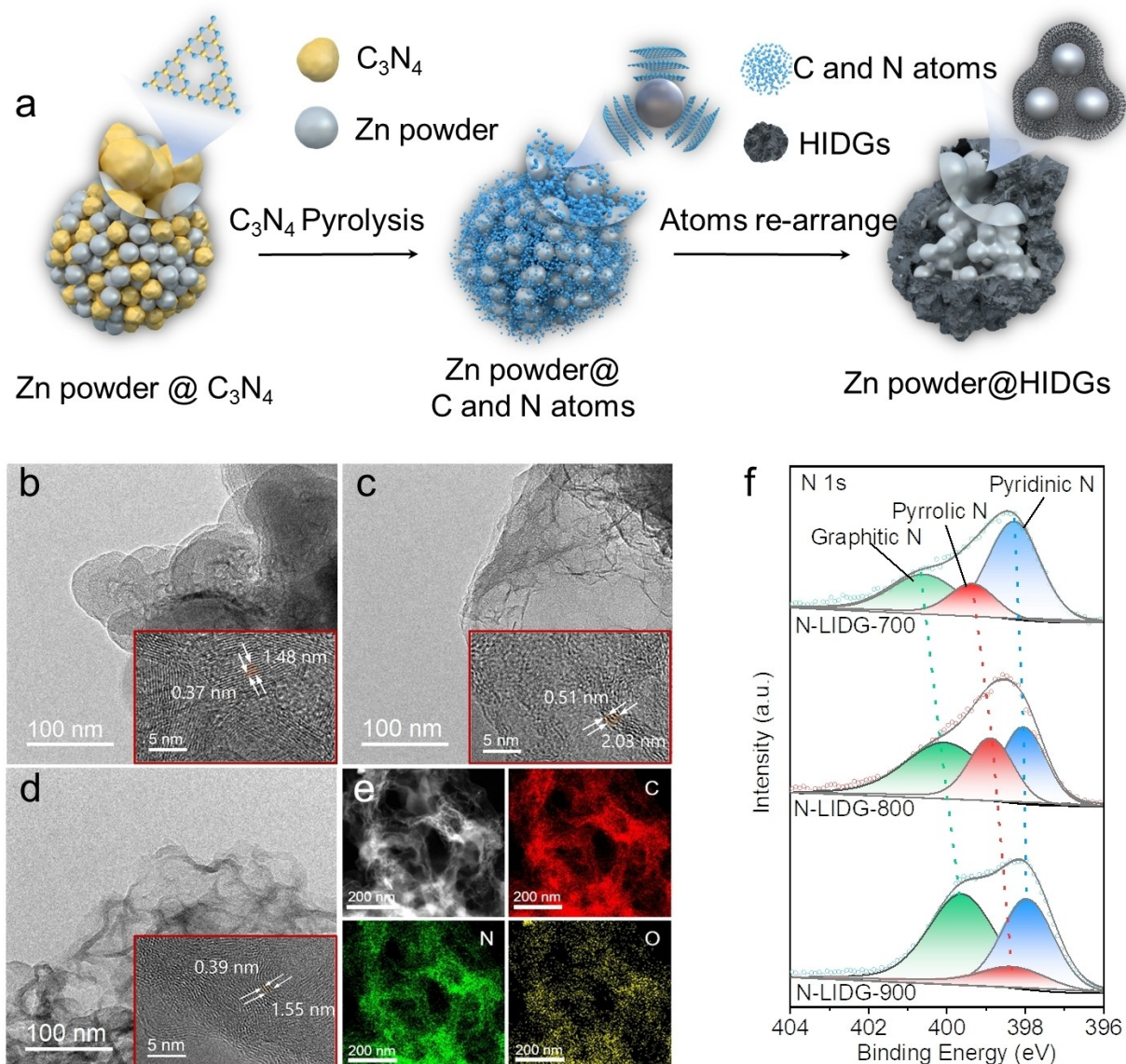
Figure 1. a) The illustration of synthesis of N-LIDGs. b-d) TEM images of b) N-LIDG-700, c) N-LIDG-800, d) N-LIDG-900 (the insets are corresponding to high-resolution TEM images of N-LIDGs). e) TEM image of N-LIDG-800 and the corresponding C, N, O elements EDX mappings. f) XPS spectra of N 1s of N-LIDGs.

respectively. The clear characteristic peaks confirm the presence of N and O atoms.[20] For the quantitative analysis, the nitrogen contents are calculated to be 24.50 %, 19.77 %, and 14.49 % for N-LIDG-700, N-LIDG-800, N-LIDG-900, respectively, and N-LIDG-800 has an oxygen loading of 4.23 %. According to the N 1s profiles of the XPS spectra (Figure 1 f, detailed in Table S2), pyridinic N (398.2 eV), pyrrolic N (399.4 eV) and graphitic N (400.9 eV) can be detected in three samples.[19] It is noteworthy that graphitic N in graphene layer with two single electrons on two p orbitals are extremely stable for graphitic structure.[20] Meanwhile, pyrrolic N widens the interlayer distance due to electrostatic repulsion when it has a single pair of electrons perpendicular to the graphene plane.[21] The nitrogen element in N-LIDG-800 is largely graphitic N with a weight ratio of 42.7 % compared to N-LIDG-700 and N-LIDG-900, suggesting that the graphitic structure appears to be dominant nitrogen element presented in the graphene layer. The stable graphitic structure and improved electrical conductivity of the carbon material are both greatly enhanced by the high concentration of graphitic N. Furthermore, the content of pyrrolic N in N-LIDG-800 (29.2 %) is much higher than that of the N-LIDG-700 (15.4 %) and N-

LIDG-900 (13.1 %), corresponding to the expansion of the layer spacing.

As an essential part, the electrolyte provides the cations and anions required in the reaction process of DIBs. Additionally, the electrochemical performance of DIBs is directly impacted by the properties of electrolyte and electrode interfaces. It makes the compatibility and kinetics of the electrolyte and graphite electrode crucial. The short board of electrolyte in DIBs can be ascribed to two main reasons. First, the continuous formation of solid electrolyte interphase (SEI) and cathode/electrolyte interphase (CEI) on electrodes may consume many cations and anions. Second, the adverse solvation structure between the solvent molecules and cations/anions may result in sluggish reaction process for ion intercalation.

To investigate the effect of electrolyte to DIBs, the solvation energies of $LiPF_6$ in PC or EC solvent have been calculated by the first principles method. The optimized solvation structures with different coordination numbers are shown in Figure 2a. The solvation energies of PF_6^- exhibit a downward trend with the increasing coordination numbers in PC and EC solvents, achieving an approximately identical value at four coordination. Under the force of electric field

inside the DIBs, the cations and anions can migrate to the surfaces of the electrode. The diverse solvation energies of Li^+ and PF_6^- with solvent molecules induce cation-anion complex separated by solvation effect. Due to the fact that the solvation trend of the solvent molecules with Li^+ is always stronger than that of PF_6^-, the solvent molecules will lose anions and remain in the Li^+ solvation sheath. [22] According to the schematic depiction of the solvation structure in Figure 2b, a lot of free PF_6^- ions are assumed to be present in the electrolyte, which is advantageous for anion transportation.[22]

Besides, the cation and anion absorption processes on electrode surfaces have a major impact on reaction kinetics.[23] There are different absorption energies of Li^+ and PF_6^- on the N-LIDGs surface with various active sites as shown in Figure 2c (the absorption structure models detailed in Figure S10, (Supporting Information)). For PF_6^- anion, natural graphite, graphitic N, pyrrole N and pyrimidine N possess similar adsorption energies of -4.96, -4.79, -3.37 and -3.52 eV, respectively, indicating strong interactions between PF_6^- and electrode interfaces. For Li^+, pyrrole N and pyrimidine N also exhibit low adsorption energies of -2.77 and -3.23 eV, respectively. Conversely,
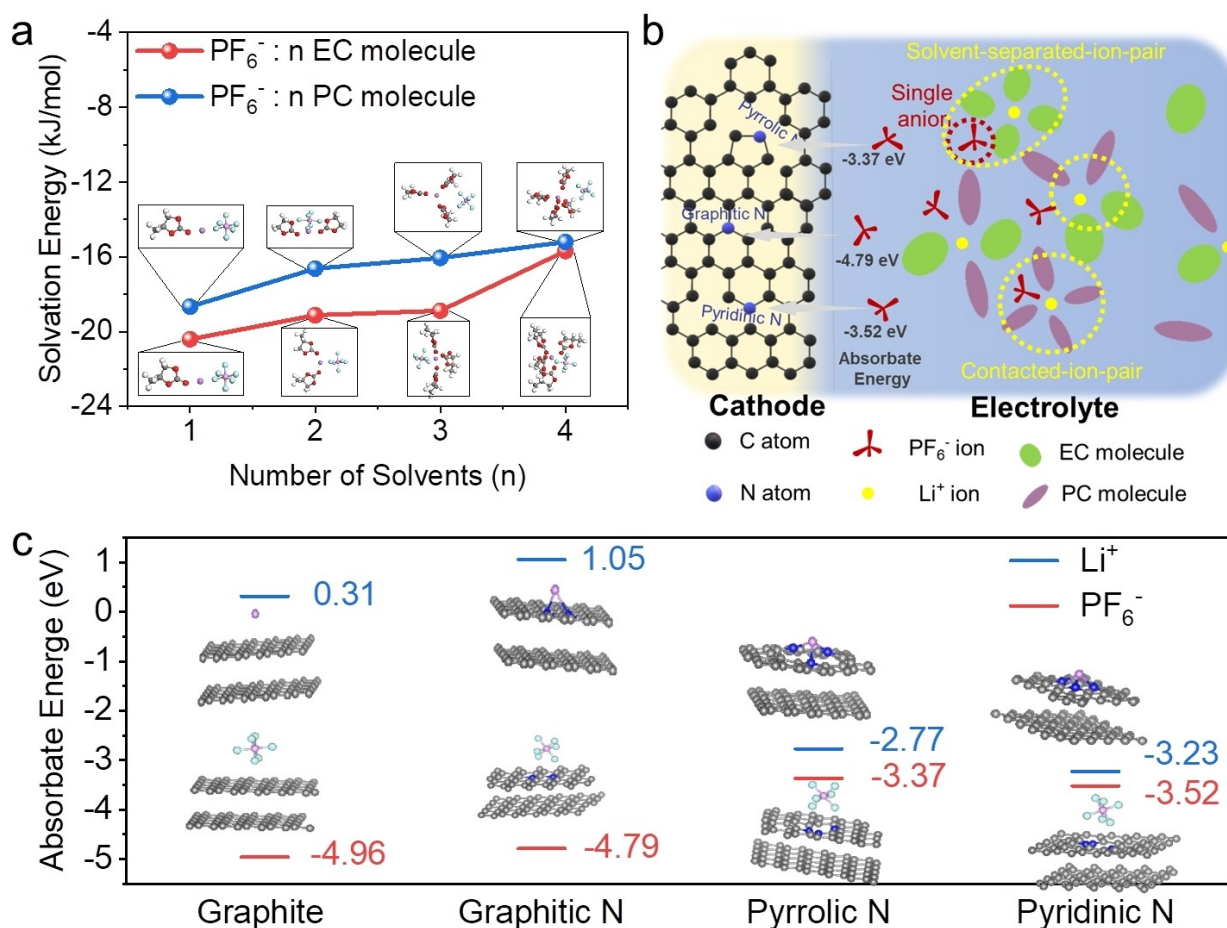
***Figure 2.*** a) The solvation structures of different number of EC or PC molecules with $LiFP_6$ and solvation energies of solvent molecules and PF_6^- with the existence of Li^+ in EC- and PC-based electrolytes, respectively. b) The diagram of solvation structures at surfaces of graphite cathodes. c) The adsorbate energies of Li^+ and PF_6^- at different types of N atoms sites and graphite surface.

Angew. Chem. Int. Ed. **2023**, *62*, e202307083 (4 of 11)

© 2023 Wiley-VCH GmbH

pristine graphite and graphitic N sites exhibit positive binding energies of 0.31 and 1.05 eV, respectively, indicating their ability to resist the ingress of Li^+ ions. These results demonstrate that the heteroatomic N doping usually has a positive effect on adsorption of Li^+ and PF_6^- on graphite electrodes. Moreover, these different active sites provide different reaction places for cations and anions, which is conducive to better structural stability.

To investigate the electrochemical performance of N-LIDGs in DIBs, we assembled Li‖N-LIDGs half cells with electrolyte of 1 M $LiPF_6$ in EC/PC (1:1 by volume). The rate capability of N-LIDGs electrodes has been tested at various current densities of 200, 300, 400, 500 and 1000 mA g^{-1} (Figure 3a), while the highest capacities of 163.8, 135.0, 120.9, 111.2 and 90.0 mAh g^{-1} can be attained by Li‖N-LIDG-800 cell compared to that of Li‖N-LIDG-700 and Li‖N-LIDG-900. When the current density returns to 200 mA g^{-1}, the Li‖N-LIDG-800 cell still recovers to a specific capacity of 173 mAh g^{-1}, implying good reversibility.

The outstanding reaction kinetics of N-LIDG-800 electrode can be attributed to the fast interface adsorption, smooth interlayer transport and high electrical conductivity, leading to improved ionic and electronic properties. The charge–discharge profiles of Li‖N-LIDG-800 cell at different current densities are shown in Figure S11, (Supporting Information). The charge–discharge profiles in the voltage range of 1.5–5.0 V of Li‖N-LIDG-800 all present ramp curves, which illustrate the synergy mechanism of diffusion behavior and capacitive characteristic for anion storage[24]. This hybrid mechanism was induced by the strong adsorption ability of micro N-LIDG-800 particles. To further verify the structural stability, the cycling property and corresponding coulombic efficiency of the Li‖N-LIDGs cells at the current density of 100 mA g^{-1} are shown in Figure 3b. After an activation of electrode interfaces, the Li‖N-LIDG-800 cell exhibits high reversible capacity more than 200 mAh g^{-1} and appreciable coulombic efficiency at least 90 % over 200 cycles. And particularly, the highest capacity
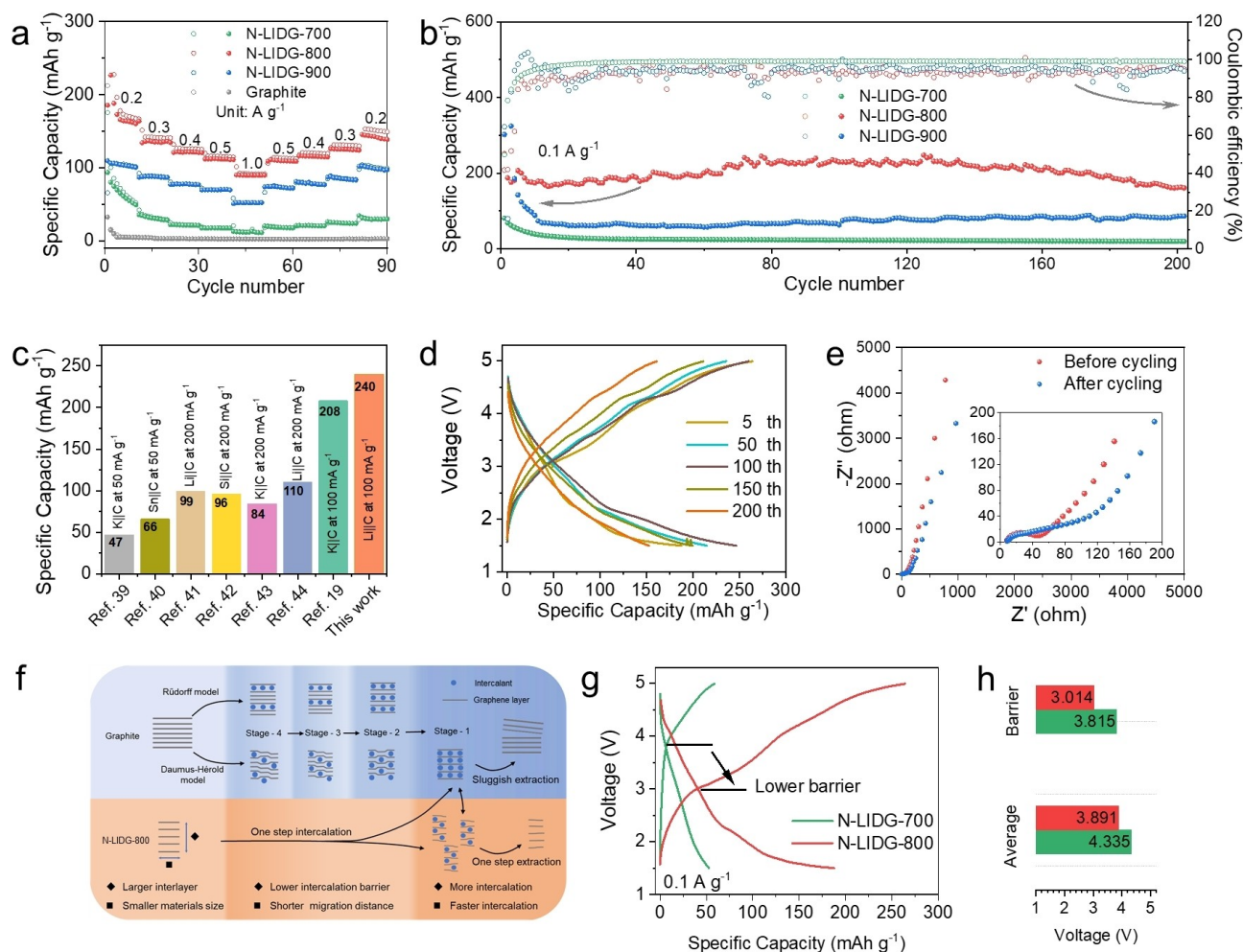
Figure 3. a) The rate capacity of N-LIDGs- and graphite-based DIBs. b) The cycle performance and corresponding coulombic efficiency of N-LIDGs-based DIBs. c) The comparison of different DIB systems at corresponding current densities. d) The charge–discharge profiles of N-LIDG-800 at the current density of 0.1 A g^{-1}. e) The electrochemical impedance spectra of N-LIDG-800 before and after cycling for 200 cycles at the current density of 0.1 A g^{-1}. f) The illustration of the different work mechanisms of graphite and N-LIDG-800 in DIBs. g) The charge–discharge profiles of N-LIDG-700 and N-LIDG-800 for the first cycle at the current density of 0.1 A g^{-1}. h) Corresponding comparison of the values of voltage plateau in g).

Angew. Chem. Int. Ed. **2023**, *62*, e202307083 (5 of 11)

© 2023 Wiley-VCH GmbH

of Li||N-LIDG-800 cell can reach 240 mAh g^{-1}, which may be the best result for DIBs so far (Figure 3c).[11,25] On the contrary, the cycling performances of Li||N-LIDG700 and Li||N-LIDG-900 cells are very poor with a rapid capacity fading to 20 and 80 mAh g^{-1}, respectively. The high reactive activity and structural stability of N-LIDG-800 electrode compared to other N-LIDGs highlight the advantages of expanded interlayer spacing and a certain proportion of nitrogen doping. As shown in Figure 3d, the charge-discharge profiles of N-LIDG-800 electrode at different cycle numbers deliver short voltage plateaus during charge-discharge processes, respectively. These voltage plateaus reveal the reversible insertion and extraction behaviors of cations and anions existed in charge–discharge processes under low current density of 100 mA g^{-1}. Nyquist plots of N-LIDG-800 and N-LIDG-700 electrode before and after cycling are displayed in Figure 3e and S12. The charge-transfer resistance R_{ct} and the ion diffusion resistance R_f are represented by a depressed semicircle at high-medium frequency and a linear region at low frequency, respectively, in the EIS data of the initial and cycled states. After cycling hundreds of times, the R_{ct} value of N-LIDG-800 electrode increases slightly, which could be explained by the fact that the ordering degree of graphite electrode is maintained. According to the electrochemical test results, unlike the Rudörff or Daumus-Hérold models described above, we speculated that the expanded interlayer structure and abundant storage sites of N-LIDG-800 can hold a large number of anions via special "deep-breathing" mechanism like lung breathing in Figure 3f. The voltage plateau of N-LIDG-800 during charging process in Figure 3g and 3 h is clearly lower than that of N-LIDG-700, indicating the easier "deep-breathing process" of anions for N-LIDG-800. Meanwhile, the N-LIDG-800 has two extinct voltage plateaus begin at 4.22 V and 2.25 V, indicating an effective discharging capacity during the discharging process. The average voltage plateau of N-LIDG-800 (2.30 V) is slightly lower than that of N-LIDG-700 (2.64 V, Figure S13).

The intercalation and diffusion of anions in cathode are significant behaviors of the DIBs which are schematically shown in Figure 4a. In the previous works, a highly upper limited voltage over 5 or 6 V is required to reach a capacity above 112 mAh g^{-1} for natural graphite electrode according to the theoretical calculation.[26] However, the graphite electrode may be in an extremely unstable state. Hence, natural graphite has a limited storage ability for anions due to the ultimate reaction thermodynamics and kinetics.

To better understand the impact of heteroatom doping carbon on the anion storage performance, the diffusion barriers of anion in N doping graphite were calculated by the DFT method (detailed in Supporting Information). Normally, it is challenging to theoretically simulate the anion diffusion behavior in natural graphite to convergence. The anions in heteroatom doping N-LIDG-800 exhibit obviously distinct diffusion barriers under diverse migration pathways with the effect of various types of N atoms, with an expanded interlayer distance of 0.47–0.51 nm. Therefore, the graphitic N leads a lower energy barrier of 0.713 eV than that of pyrrolic N (1.456 eV) and pyridinic N (1.461 eV)

(Figure 4b, detailed migration paths are shown in Figure S14, Supporting Information). These results illustrate that the presence of graphitic nitrogen in N-LIDG-800 facilitates the insertion and migration of anions and allows the storage of a larger number of anions.

To testify the mechanism of anions storage behavior of N-LIDG-800, X-ray photoelectron spectroscopy (XPS) and Fourier transfer infrared (FTIR) were carried out. Figure 4c shows the XPS of N-LIDG-800 before and after charging process. During the charging state of the cell, the high-resolution P 2p spectrum exhibits a signal for P–F bonds at 135 eV.[11] Conversely, in the discharging state, there is no signal for P–F bonds observed in the N-LIDG-800. Furthermore, the FTIR spectra of pristine and charged N-LIDG-800 electrodes are shown in Figure 4d. The feature peak of PF_6^- around wavelength of 820–850 cm^{-1} is observed in the spectrum of charged N-LIDG-800 electrode, which is absent in pristine N-LIDG-800 electrode.[11] The adsorption and intercalation behaviors of anions during the charging process are conclusively demonstrated by the aforementioned evidence.

To further reveal the reversible insertion and extraction process of Li$^+$ and PF_6^- in the N-LIDG-800 cathode, in situ Raman and in situ XRD measurements were carried out to monitor the structure and composition changes in Li||N-LIDG-800 cells. From the 2D heat map of in situ Raman spectra (Figure 4e), the initial value of I_D/I_G is 1.15, which represents the presence of a large number of defects in N-LIDG-800 at pristine state. During the charging process (up to 5.0 V), the intensity of the D peak first increases and then decreases, while the intensity change of the G peak is opposite, corresponding to a significant increase in the values of I_D/I_G to 1.2, followed by a decrease to 0.9. This phenomenon shows that anion insertion causes interlayer structure adjustment and disorder degree increases first, and subsequently, rectifies defects and improves the order degree of graphite via anion adsorption on defect sites, thus leading to a rapid reaction kinetics in initial state.[27] Moreover, the formation of single graphene layer may initiate the intensity increase of G peak during the anion insertion. In the voltage range of 3.0 to 4.5 V, the values of I_D/I_G can be retained at 0.9 due to the strong anion holding capacity in open layered structure.[28] When discharged to a low potential state (3.0 V), the value of I_D/I_G may recover to 1.1, indicating the reversible extraction of anions and highly structural stability of N-LIDG-800. More importantly, after the anion extraction, no other impure peaks are emerged, demonstrating the good reproducibility of defect-rich structure. In addition, in situ XRD was carried out to monitor the crystallinity of N-LIDG-800 during three consecutive charge-discharge cycles. As shown in Figure 4f, the intensity of diffraction peak (002) was significantly weakened at each fully charged states (red dash) with high depth of charge (DOC, ≈100 %, corresponding voltage curves as shown in Figure S15), This phenomenon reflects that anions are completely inserted into graphite interlayers to reduce the crystallinity of N-LIDG-800. Specifically, the locations of diffraction peak (002) and its splitting peak are immobile during the charge-discharge processes, indicating that the
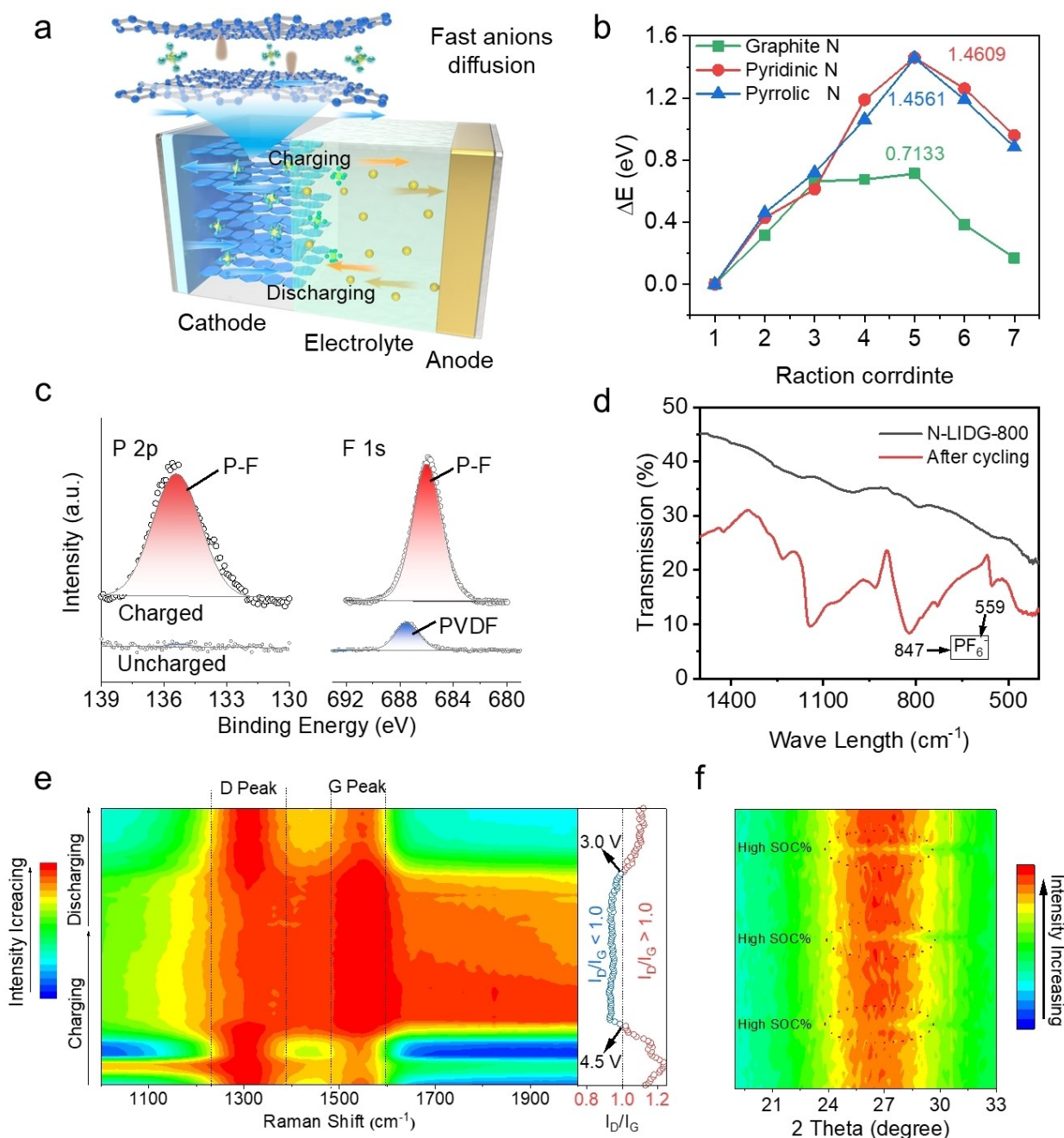
Figure 4. a) The schematic of the DIB mechanism and ion transmission. b) The migration energy of PF_6^- ion migration over different types of N atoms. c) The XPS of P 2p and F 1s of N-LIDG-800 cathodes before and after cycling for 200 cycles at 0.1 A g^{-1}. d) The FTIR spectra of C—C P—F on N-LIDG-800 cathodes before and after cycling for 200 cycles at 0.1 A g^{-1}. e) The in situ Raman spectra of N-LIDG-800 cathode when cycling at the current density of 0.1 A g^{-1}. f) The in situ XRD spectra of N-LIDG-800 cathode when cycling at current density of 0.1 A g^{-1}.

distance of the graphite interlayer is fixed without a common expansion-contraction process, corresponding to a fast reaction kinetics and stable structure. These evidences of in situ XRD confirm the above speculation about the "deep-breathing" mechanism for anion storage.

To further investigate the kinetic processes in half-cells, the cyclic voltammetry (CV) test of Li||N-LIDG-800 cell was carried out at various scan rates. As displayed in

Figure 5a, the distinct redox peaks during the charge-discharge process reveal the electrochemical oxidation (anions intercalation reaction) and reduction (anions extraction reaction) existed in N-LIDG-800 cathode. The relationship between scan current (i) and scan rate (v) can be expressed as $i = a\,v^b$ Where a and b are two adjustable coefficients. The b value can be defined by the linear relationship between the $log\,v$ and $log\,i$, where $b = 0.5$ is
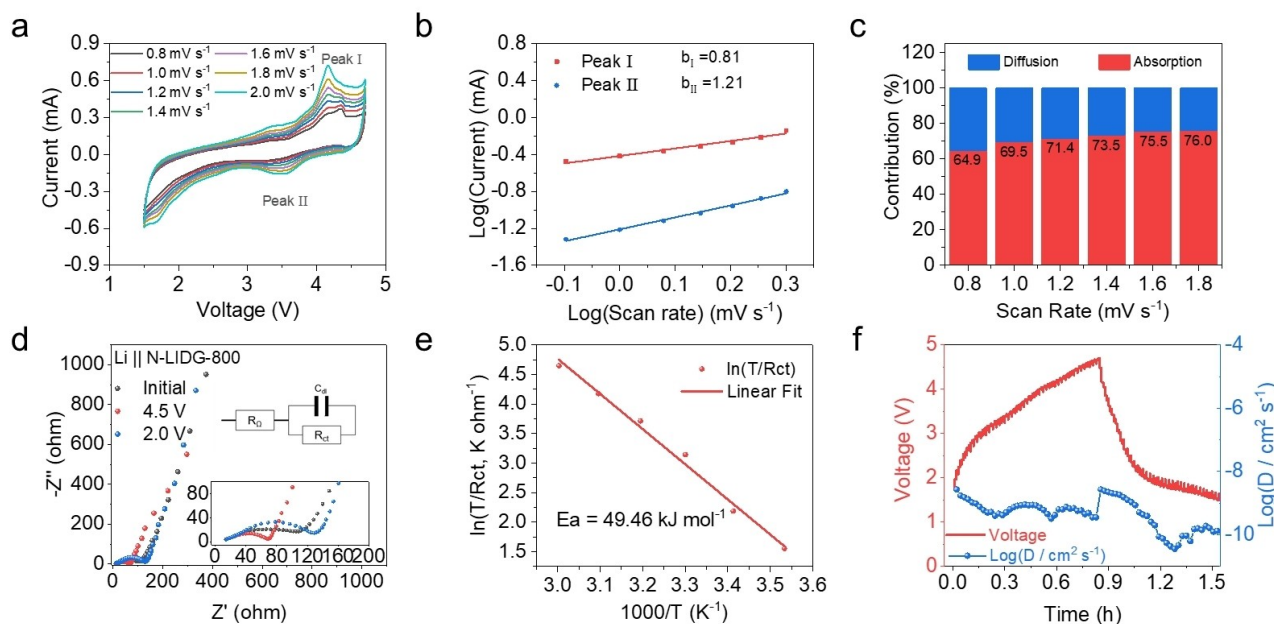
Figure 5. a) The Cyclic voltammogram of N-LIDG-800 based DIBs at different scan rates and corresponding b) contribution of pseudo-capacity of N-LIDG-800 cathode. c) The diffusion and absorption contribution of cyclic voltammetry test at different scan rates from 0.8 to 1.8 mV s^{-1}. d) The EIS profiles of N-LIDG-800 cathodes at different open circuit potentials. e) The activation energy of N-LIDG-800 calculated by Arrhenius equation. f) The GITT profiles and corresponding diffusion coefficient of PF$_6^-$ ions in N-LIDG-800 cathode.

related to a diffusion controlled kinetic behavior, while $b=1$ represents a capacitive contribution kinetic behavior.[29] The b values of N-LIDG-800 are calculated to be 0.81 and 1.29 (Figure 5b), demonstrating the fast charge storage process achieved by the advantageous capacitance effect and negligible ion diffusion in bulk. Meanwhile, the capacitive and diffusion-dominated contributions of the N-LIDG-800 electrode were quantitatively calculated according to the proportion of k_1v and $k_2v^{1/2}$ at various voltages, respectively, which can be separated via the following equation as $i=k_1v+k_2v^{1/2}$.[30] Figure 5c shows the capacitive and diffusion contributions of N-LIDG-800 electrode at different scan rates from 0.8 to 1.8 mV s^{-1}, corresponding to the increase of capacitive contributions from 64.9% to 76.0% (detailed in Figure S16, Supporting Information). These results prove that the outstanding rate performance and cycling durability of the N-LIDG-800 cathodes can be closely associated to the great capacitive contribution especially at high rates. However, the capacitive contribution was only 32.16% at extremely low scan rate of 0.1 mV s^{-1}, indicating the sufficient time for the convenient intercalation reaction during the slow charging process (Figure S17, Supporting Information).

Furthermore, the EIS was employed to analyze the kinetic performance of the Li‖N-LIDG cell (Figure 5d). The significantly decreased R_{ct} value of 69.2 Ω can be attained at fully charged state (4.5 V) compared to that of open-circuit-voltage state (108.2 Ω) and fully discharged state (131.2 Ω), implying that the slow charge transfer process during initial charging and discharging stages are regarded as main speed-determination step. Then, the R_{ct}

values of Li‖N-LIDG-800 cell tested at different temperatures were obtained from the temperature-change EIS to investigate the activation capacity of Li$^+$ or PF$_6^-$ ions through the SEI layer (the EIS spectra shown in Figure S18, Supporting Information). According to the Arrhenius equation:[31]

$$1/R_{ct} = A\,\exp(-E_a/RT)$$

Amongst, the symbols A, E_a, R, and T denote the frequency factor, activation energy, gas constant, and absolute temperature, respectively. The low activation energy of 49.46 kJ mol^{-1} was evaluated from the slope of the lnR$_{ct}^{-1}$–1/T plots as shown in Figure 5e, illustrating that the electrolyte of LiPF$_6$ in EC: PC for DIBs exhibits slightly better kinetics than that of EC based electrolyte for LIBs. This phenomenon is consistent with the previous calculation results.

To evaluate anion diffusion coefficient (D$_{PF_6^-}$) in N-LIDG cathode, the galvanostatic intermittent titration technology (GITT) was employed at the current density of 0.3 A g^{-1} (Figure 5f). The diffusion coefficient of anion can be calculated by the following equation:

$$D_{PF_6} = \frac{4}{\pi}\left(\frac{iV_m}{AF_Z}\right)^2\left[\left(\frac{dE}{d\delta}\right)\Big/\frac{dE}{d\sqrt{t}}\right]^2$$

In this equation, i is the value of current in test process, V_m is the molar volume of electrode, is F is Faraday's constant of 96485 C/mol, A is the contact area of electrode and electrolyte, Z_A is charge number of ions and takes the

value of 1 here, $dE/d\delta$ is slope of the coulometric titration curve, and E is the potential of tested cell.[32]

The diffusion rate of anion was calculated by a single-step GITT measurement. The thermodynamic equilibrium potentials are close to the charging and discharging curves, suggesting that the risk of lithium precipitation is low. The corresponding diffusion coefficients of anion in the N-LIDG-800 are in the range of 10^{-10}–10^{-9} cm^{2}s^{-1}, which is consist with that of lithium diffusion coefficient in oxide active materials.[33] The low diffusion barrier and broad diffusion channel of N-LIDG-800 promote anion transmission.

Finally, to verify the electrochemical performance of the N-LIDG-800 electrode in the DCBs, the coin-cells and pouch cells were assembled using pre-lithiated N-LIDG-800 anode. The electrochemical performance of the DCBs cell was calculated based on all the active materials of positive and negative electrode. The cycling performance and corresponding coulombic efficiency of N-LIDG-800||N-LIDG-800 coin-cell are shown in Figure 6a. The initial discharge capacity of the cell at the current density of 1.0 A g^{-1} was 64 mAh g^{-1} while applying N-LIDG-800 as

both the cathode and anode materials for the DCBs. Moreover, after 2400 cycles of long-term cycling, 75% of the capacity of DCB was remained with cycling efficiency of 83% throughout the cycling process. By analyzing the charge-discharge curves, as shown in Figure S19 (Supporting Information), it can be obtained that the average discharge voltage distribution of the DCBs during cycling is 3.5–3.9 V, showing a high discharge voltage plateau, which has a positive impact on the energy density of the battery.

In addition, we explored the large-scale application of N-LIDG-800-based DCBs by assembling N-LIDG-800||N-LIDG-800 pouch cell as shown in Figure 6b. The cycling performance of the pouch cell between voltage window of 1.5–5 V as shown in Figure 6c. The initial capacity of the pouch cell is 67.6 mAh g^{-1} and over half-capacity can be remained after cycling test at the current density of 0.25 A g^{-1}, demonstrating the promising potential for low-cost, and large-scale energy storage devices. Furthermore, the N-LIDG-800||N-LIDG-800 pouch cell successfully lighten the bulbs as illustrated in Figure 6d. The N-LIDG-800||N-LIDG-800 pouch cell exhibits outstanding performance whether used in series or parallel circuits, demonstrat-
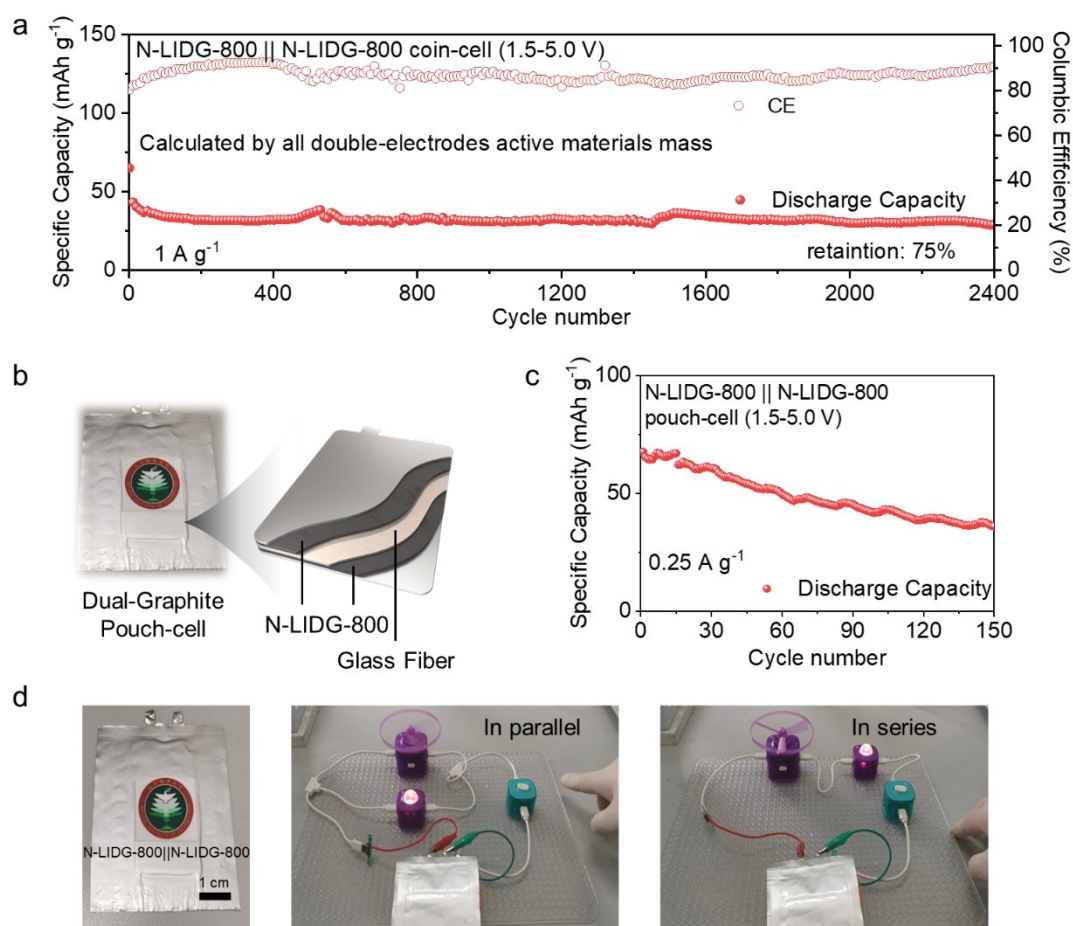
Figure 6. a) The cycling performance and corresponding coulombic efficiency of N-LIDG-800||N-LIDG-800-coin cell. b) Illustration of N-LIDG-800||N-LIDG-800 pouch cell. c) The cycling performance and corresponding coulombic efficiency of N-LIDG-800||N-LIDG-800 pouch cell. d) The pictures of N-LIDG-800||N-LIDG-800 pouch cell and the application of N-LIDG800||N-LIDG800 pouch cell for lightening a bulb and a fan in parallel and in series respectively.

ing the practicality and significance of DCBs in future practical energy storage applications.

In summary, a heteroatoms-doping graphite material with large interlayer distance was constructed and employed as active electrode materials in DIBs and DCBs. The higher layer spacing allows for more anion storage spaces in the N-LIDG-800 cathode. Theoretical computations were employed to reveal the reduced energy barriers for insertion and migration of anions in the interlayers. Moreover, the heteroatom doping not only has a favorable impact on ionic adsorption but also greatly improve the reaction kinetics. A firm The combination of multiple advantages allows for an efficient and stable energy storage mechanism in the DIBs. Therefore, the N-LIDG-800-based DIBs achieved the highest capacity of $240\ mAh\,g^{-1}$ and had an impressive cycle performance more than 2400 times. Noteworthy, a practical DCB has been developed to attain a high energy density and low cost. This work provides a new insight into the anion storage mechanism of DIBs, as well as a feasible design strategy for capacity enhancement and overall performance improvement has been proposed.

Conclusion

In summary, a heteroatoms-doping graphite material with large interlayer distance was constructed and employed as active electrode materials in DIBs and DCBs. The higher layer spacing allows for more anion storage spaces in the N-LIDG-800 cathode. Theoretical computations were employed to reveal the reduced energy barriers for insertion and migration of anions in the interlayers. Moreover, the heteroatom doping not only has a favorable impact on ionic adsorption but also greatly improve the reaction kinetics. The combination of multiple advantages allows for an efficient and stable energy storage mechanism in the DIBs. Therefore, the N-LIDG-800-based DIBs achieved the highest capacity of $240\ mAh\,g^{-1}$ and had an impressive cycle performance more than 2400 times. Noteworthy, a practical DCB has been developed to attain a high energy density and low cost. This work provides a new insight into the anion storage mechanism of DIBs, as well as a feasible design strategy for capacity enhancement and overall performance improvement has been proposed.

Acknowledgements

Conflict of Interest

The authors declare no conflict of interest.

Data Availability Statement

The data that support the findings of this study are available in the supplementary material of this article.

[1] a) J.-M. Tarascon, M. Armand, *Nature* **2001**, *414*, 359–367; b) S. Chu, Y. Cui, N. Liu, *Nat. Mater.* **2017**, *16*, 16–22.

[2] a) M. Winter, R. J. Brodd, *Chem. Rev.* **2004**, *104*, 4245–4270; b) B. Dunn, H. Kamath, J.-M. Tarascon, *Science* **2011**, *334*, 928.

[3] D. Larcher, J. M. Tarascon, *Nat. Chem.* **2015**, *7*, 19–29.

[4] a) F. P. McCullough, C. A. Levine, R. V. Snelgrove, *US 4830938* **1989**; b) T. Placke, O. Fromm, S. F. Lux, P. Bieker, S. Rothermel, H.-W. Meyer, S. Passerini, M. Winter, *J. Electrochem. Soc.* **2012**, *159*, A1755; c) L. Zhang, H. Wang, X. Zhang, Y. Tang, *Adv. Funct. Mater.* **2021**, *31*, 2010958.

[5] T. Placke, A. Heckmann, R. Schmuch, P. Meister, K. Beltrop, M. Winter, *Joule* **2018**, *2*, 2528–2550.

[6] a) K. Yang, L. Jia, X. Liu, Z. Wang, Y. Wang, Y. Li, H. Chen, B. Wu, L. Yang, F. Pan, *Nano Res.* **2020**, *13*, 412–418; b) M. Wang, Y. Tang, *Adv. Energy Mater.* **2018**, *8*, 1703320.

[7] a) U. Hofmann, W. Rüdorff, *Trans. Faraday Soc.* **1938**, *34*, 1017–1021; b) C. Sole, N. E. Drewett, L. J. Hardwick, *Faraday Discuss.* **2014**, *172*, 223–237.

[8] J. Xu, Y. Dou, Z. Wei, J. Ma, Y. Deng, Y. Li, H. Liu, S. Dou, *Adv. Sci.* **2017**, *4*, 1700146.

[9] a) T. Ishihara, Y. Yokoyama, F. Kozono, H. Hayashi, *J. Power Sources* **2011**, *196*, 6956–6959; b) J. A. Read, *J. Phys. Chem. C* **2015**, *119*, 8438–8446; c) K. V. Kravchyk, P. Bhauriyal, L. Piveteau, C. P. Guntlin, B. Pathak, M. V. Kovalenko, *Nat. Commun.* **2018**, *9*, 4469.

[10] a) W. Märkle, N. Tran, D. Goers, M. E. Spahr, P. Novák, *Carbon* **2009**, *47*, 2727–2732; b) W. Märkle, J.-F. Colin, D. Goers, M. E. Spahr, P. Novák, *Electrochim. Acta* **2010**, *55*, 4964–4969.

[11] K. Yang, Q. Liu, Y. Zheng, H. Yin, S. Zhang, Y. Tang, *Angew. Chem. Int. Ed.* **2021**, *60*, 6326–6332.

[12] a) L. Qie, W. Chen, X. Xiong, C. Hu, F. Zou, P. Hu, Y. Huang, *Adv. Sci.* **2015**, *2*, 1500195; b) J. Yang, X. Zhou, D. Wu, X. Zhao, Z. Zhou, *Adv. Mater.* **2017**, *29*, 1604108.

[13] Y. Wen, K. He, Y. Zhu, F. Han, Y. Xu, I. Matsuda, Y. Ishii, J. Cumings, C. Wang, *Nat. Commun.* **2014**, *5*, 4033.

[14] J. Liu, Y. Zhang, L. Zhang, F. Xie, A. Vasileff, S.-Z. Qiao, *Adv. Mater.* **2019**, *31*, 1901261.

[15] J. Liu, Y. Zhang, L. Zhang, F. Xie, A. Vasileff, S. Z. Qiao, *Adv. Mater.* **2019**, *31*, 1901261.

[16] M. Pimenta, G. Dresselhaus, M. S. Dresselhaus, L. Cancado, A. Jorio, R. Saito, *Phys. Chem. Chem. Phys.* **2007**, *9*, 1276–1290.

[17] A. C. Ferrari, *Solid State Commun.* **2007**, *143*, 47–57.

[18] Z. Q. Liu, H. Cheng, N. Li, T. Y. Ma, Y. Z. Su, *Adv. Mater.* **2016**, *28*, 3777–3784.

[19] S. Hussain, R. Amade, E. Jover, E. Bertran, *J. Mater. Sci.* **2013**, *48*, 7620–7628.

[20] a) Q. Wei, X. Tong, G. Zhang, J. Qiao, Q. Gong, S. Sun, *Catalysts* **2015**, *5*, 1574–1602; b) A. Dettlaff, M. Sawczak, E.

Klugmann-Radziemska, D. Czylkowski, R. Miotk, M. Wila-mowska-Zawłocka, *RSC Adv.* **2017**, *7*, 31940–31949.

[21] a) D. Wei, Y. Liu, Y. Wang, H. Zhang, L. Huang, G. Yu, *Nano Lett.* **2009**, *9*, 1752–1758; b) S. Wang, L. Xia, L. Yu, L. Zhang, H. Wang, X. W. Lou, *Adv. Energy Mater.* **2016**, *6*, 1502217.

[22] L. Xing, X. Zheng, M. Schroeder, J. Alvarado, A. von Wald Cresce, K. Xu, Q. Li, W. Li, *Acc. Chem. Res.* **2018**, *51*, 282–289.

[23] a) T. Zhou, J. Shen, Z. Wang, J. Liu, R. Hu, L. Ouyang, Y. Feng, H. Liu, Y. Yu, M. Zhu, *Adv. Funct. Mater.* **2020**, *30*, 1909159; b) Z. Li, J. Lin, B. Li, C. Yu, H. Wang, Q. Li, *J. Energy Storage* **2021**, *44*, 103437.

[24] N. Wu, W. Yao, X. Song, G. Zhang, B. Chen, J. Yang, Y. Tang, *Adv. Energy Mater.* **2019**, *9*, 1803865.

[25] a) K. Beltrop, S. Beuker, A. Heckmann, M. Winter, T. Placke, *Energy Environ. Sci.* **2017**, *10*, 2090–2094; b) B. Ji, F. Zhang, X. Song, Y. Tang, *Adv. Mater.* **2017**, *29*, 1700519; c) G. Wang, M. Yu, J. Wang, D. Li, D. Tan, M. Löffler, X. Zhuang, K. Müllen, X. Feng, *Adv. Mater.* **2018**, *30*, 1800533; d) C. Jiang, L. Xiang, S. Miao, L. Shi, D. Xie, J. Yan, Z. Zheng, X. Zhang, Y. Tang, *Adv. Mater.* **2020**, *32*, 1908470; e) X. Li, X. Ou, Y. Tang, *Adv. Energy Mater.* **2020**, *10*, 2002567; f) X. Tong, X. Ou, N. Wu, H. Wang, J. Li, Y. Tang, *Adv. Energy Mater.* **2021**, *11*, 2100151.

[26] X. Zhou, Q. Liu, C. Jiang, B. Ji, X. Ji, Y. Tang, H. M. Cheng, *Angew. Chem. Int. Ed.* **2020**, *59*, 3802–3832.

[27] M. Ammar, N. Galy, J. Rouzaud, N. Toulhoat, C. Vaudey, P. Simon, N. Moncoffre, *Carbon* **2015**, *95*, 364–373.

[28] J. C. Chacón-Torres, L. Wirtz, T. Pichler, *ACS Nano* **2013**, *7*, 9249–9259.

[29] C. Choi, D. S. Ashby, D. M. Butts, R. H. DeBlock, Q. Wei, J. Lau, B. Dunn, *Nat. Rev. Mater.* **2020**, *5*, 5–19.

[30] a) T. C. Liu, W. Pell, B. Conway, S. Roberson, *J. Electrochem. Soc.* **1998**, *145*, 1882; b) J. Wang, J. Polleux, J. Lim, B. Dunn, *J. Phys. Chem. C* **2007**, *111*, 14925–14931.

[31] D. Wu, J. He, J. Liu, M. Wu, S. Qi, H. Wang, J. Huang, F. Li, D. Tang, J. Ma, *Adv. Energy Mater.* **2022**, *12*, 2200337.

[32] a) W. Weppner, R. A. Huggins, *J. Electrochem. Soc.* **1977**, *124*, 1569; b) C. J. Wen, B. A. Boukamp, R. A. Huggins, W. Weppner, *J. Electrochem. Soc.* **1979**, *126*, 2258.

[33] D. W. Dees, S. Kawauchi, D. P. Abraham, J. Prakash, *J. Power Sources* **2009**, *189*, 263–268.